Systematic Synthesis and Design of Ultralow Threshold 2:1 Parametric Frequency Dividers

Hussein M. E. Hussein, *Student Member, IEEE*, Mahmoud A. A. Ibrahim, *Student Member, IEEE*, Giuseppe Michetti, *Student Member, IEEE*, Matteo Rinaldi, *Senior Member, IEEE*, Marvin Onabajo, *Senior Member, IEEE*, and Cristian Cassella, *Member, IEEE*

***Abstract*— A new method is discussed for the systematic synthesis, design, and performance optimization of single-ended varactor-based 2:1 parametric frequency dividers (PFDs) exhibiting an ultralow-power threshold (P_{th}). For the first time, it is analytically shown that the P_{th}-value exhibited by any PFD can be expressed as an explicit closed-form function of the different impedances forming its network. Such a unique and unexplored property permits reliance on linear models, during PFD design and performance optimization. The validity of our analytical model has been verified, in a commercial circuit simulator, through the time- and frequency-domain algorithms. To demonstrate the effectiveness of our new synthesis approach, we also report on a lumped prototype of a 200:100 MHz PFD, realized on a printed circuit board (PCB). Although inductors with quality factors lower than 50 were used, the PFD prototype exhibits a P_{th}-value lower than −15 dBm. Such a P_{th}-value is the lowest one ever reported for passive varactor-based PFDs operating in the same frequency range.**

***Index Terms*— Auxiliary generators (AGs), frequency dividers, linear-time-variant (LTV) system, nonlinear dynamics.**

I. Introduction

In THE last decades, growing attention has been paid to the development of new electronic components leveraging strong nonlinear dynamics in order to surpass the limitations of currently available devices and systems [1]–[12]. In particular, many research groups have looked at the possibility of exploiting nonlinear phenomena to attain frequency synthesizers (FSs) with record-low jitter levels [9], [13]–[20]. Only recently, one of the investigated approaches produced a new CMOS-compatible component referred to as parametric filter (PFIL) [21], [22], which shows the unprecedented ability to act as a jitter cleaner without requiring the use of a voltage-controlled oscillator (VCO). PFILs leverage the complex nonlinear dynamics exhibited by varactor-based 2:1 parametric frequency dividers (PFDs) [23]–[26], placed in nonautonomous feedback loops and directly connected at the output of a noisy FS. Despite the fact that a PFIL prototype showing a large phase-noise suppression was recently demonstrated [22], such a system is characterized by a power consumption that is not suitable for low-power integrated electronics. For this reason, new strategies to reduce the power consumed by PFILs are required to enable their adoption in low-power systems. This critical power limitation is mostly determined by the minimum input power (P_{th}) that makes PFDs able to operate in their division regime. PFDs are nonlinear circuits that rely on the adoption of modulated reactances to activate a frequency-division mechanism. Because of their strong nonlinear behavior, the design of PFDs, through commercial circuit simulators, presents several challenges that have prevented achieving PFDs exhibiting ultralow P_{th}-values [16], [24]. For instance, as these devices can exhibit abrupt changes in their electrical characteristics, the use of time-domain (TD) algorithms to model their response is only limited to PFDs using a reduced number of components. This constraint impedes the attainment of optimized PFD designs with minimum P_{th}-values through TD-based methods. In contrast, the detection of subharmonic oscillations through conventional harmonic-balance (HB) algorithms shows severe limitations due to the absence of subharmonic frequencies among those used to find the steady-state solution of time-varying circuits. In order to circumvent these limitations, several approaches were developed to detect the onset of subharmonic oscillations in PFDs, through perturbation methods [12], [27], [28] or through the iterative determination of the conversion matrix [29]–[32] associated with any adopted variable reactance. Also, a recent effort has even produced a new methodology to reconstruct the bifurcation loci of nonlinear RF circuits without recurring to continuation techniques [33]. Although several techniques are now available to detect the presence of large-signal periodic oscillations in different types of circuits, a systematic approach to design PFDs with minimum P_{th} value is still to be fully developed.

Recently, while investigating the optimum design conditions to build nonreciprocal RF filters [34] through a network of modulated reactances, we discovered that it is always possible to express the transfer function describing the operation of such systems as an explicit function of the static equivalent impedance seen by each modulated component. The discovery of such a unique property led to augmented synthesis capabilities that allowed us to unveil the main design

Manuscript received February 21, 2020; revised April 25, 2020 and May 26, 2020; accepted May 30, 2020. Date of publication June 18, 2020; date of current version August 5, 2020. This work was supported by the National Science Foundation (NSF) under Grant 1854573. *(Corresponding author: Hussein M. E. Hussein.)*

The authors are with the Department of Electrical and Computer Engineering, College of Engineering, Northeastern University, Boston, MA 02115 USA (e-mail: h.hussein@northeastern.edu).

Color versions of one or more of the figures in this article are available online at http://ieeexplore.ieee.org.

Digital Object Identifier 10.1109/TMTT.2020.2999790

criteria and functionalities of a novel nonreciprocal RF component, with optimized architecture, insertion loss, and isolation. Here, we show that a similar property exists for PFDs, relating the stability of large-signal periodic regimes to the different static impedances forming their network. For the first time, a closed-form expression of the P_{th}-value exhibited by any 2:1 varactor-based PFD is derived and reported. In particular, we show that this key performance parameter can indeed be expressed as an explicit function of the impedances seen by the variable reactance toward the PFD circuit ports and relative to the input (or pump, f_{pump}) and output (f_{out}) frequencies. Therefore, we demonstrate that the minimization of P_{th} can be tackled through standard impedance synthesis approaches, thereby not requiring the adoption of perturbation-based or iterative techniques that are often hard to use without increasing the design and the simulation complexity. This complexity can even be unsustainable when targeting ultrahigh-frequency (UHF) and superhigh-frequency (SHF) PFDs, whose design requires electromagnetic simulations to account and compensate for the significant parasitics generally introduced by the board layout. Due to the derived closed-form expression of P_{th}, a new design guideline for ultralow threshold PFDs is unveiled and reported, hence providing the means to finally achieve low-power PFILs. To demonstrate the validity and effectiveness of our findings, a 200:100 MHz PFD, using lumped off-the-shelf components, was designed and built on a printed circuit board (PCB). Even though this device uses inductors with quality factors (Q) lower than 50, the engineered strategic selection of its passive components renders it able to achieve a P_{th}-value lower than -15 dBm. To the best of the authors' knowledge, this value is the lowest one ever reported for passive PFDs operating in the same frequency range [16], [24], [25], [29].

II. Detection of Subharmonic Oscillations in PFDs

The detection of parametric instabilities represents a significant challenge for most commercial circuit simulators [24]. In particular, a reliable identification of subharmonic oscillations would not only enable optimal performance in parametric circuits but would also allow the prevention of drops in spectral purity and power efficiency in other circuit components, such as amplifiers and frequency multipliers [33], [35], [36]. Several research groups have looked at possible approaches to identify the generation of parametric oscillations in RF systems. Some approaches use TD algorithms. However, due to the abrupt functional changes occurring at points of marginal stability, the use of TD-based detection methods to analyze the operation of parametric circuits may lead to severe convergence issues. These problems can be only overcome through the adoption of finer time steps, which frequently implies unsustainable computation times. For this reason, their use can even be impossible when analyzing complex systems, such as PFILs or more advanced PFD designs. On the other hand, when using frequency-domain (FD)-based algorithms, most commercial HB-circuit simulators cannot detect the onset of oscillations occurring at frequencies that are submultiples of any applied input frequency. This is due to the lack of subharmonic frequencies among those used by these simulators to evaluate currents and voltages in analyzed circuits. However, as FD methods can efficiently characterize the behavior of any circuit with a much shorter computation time than TD methods, enabling their use is key to most efficiently designed PFDs. Therefore, different approaches have been explored to achieve a reliable behavioral prediction of parametric components and systems through HB methods. In particular, in [37], a voltage–auxiliary generator technique was developed to extract the P_{th}-value attained by varactor-based PFDs. This approach is based on the artificial introduction of a voltage generator in series with an ideal frequency-selective resistive filter and placed in parallel to the adopted modulated reactance. This generator, which is characterized by an excitation frequency equal to the divided output frequency (f_{out}), applies a low-voltage signal in the circuit, thus forcing any HB simulator to consider a signal at f_{out} during its computation. The signal generated by the auxiliary generator (AG) acts as noise, characterized by an impulsive frequency distribution centered at f_{out}. Its use permits the assessment of PFD stability, at f_{out}, as the amplitude of the main excitation voltage, at f_{pump} (i.e., $2f_{\text{out}}$), is increased. Although this method allows the detection of any parametric instability, it requires iterative simulation steps to find the steady-state response of PFDs, after these systems transition into their division region. As an alternative approach, a novel detection technique has recently been developed [16]. This is based on the introduction of a power auxiliary generator (pAG) in the PFD output mesh and on behalf of the PFD output load (R_L). A pAG is characterized by an ideal voltage generator, at f_{out}, in series with its internal impedance (Z_g, set to be equal to R_L). The available power (P_{sub}) of the pAG is kept small enough to ensure that no perturbation of the circuit behavior is generated as a result of its use. Thus, the introduction of the pAG allows the inclusion of f_{out} in the list of frequencies used by any HB simulator, without perturbing the impedances seen by any modulated reactance in the circuit. Furthermore, contrary to the AG, the use of a pAG avoids reliance on optimizations to extract the steady-state response of PFDs. In fact, when a pAG is used, the PFD output voltage can be directly extracted from the HB-simulated voltage across the pAG at f_{out}. Such a voltage automatically differs from the originally set value, corresponding to P_{sub}, after the onset of any subharmonic oscillation at f_{out} in the circuit. This unique feature enables the direct extraction of the PFD output spectrum even for input power (P_{in}) levels that are higher than P_{th}. However, in order to reliably use the discussed pAG technique, very fine sweeps of specific controlling parameters, such as P_{in} or f_{pump}, must still be implemented to facilitate the HB convergence to nontrivial dividing solutions. This feature also makes the pAG technique nonideal when optimizing PFD designs targeting ultralow P_{th}-values. Hence, when the minimization of P_{th} is the main design objective, gaining intuition about the different factors affecting its value is fundamental. To do so, one of objectives of this article has been to compute a generic closed-form expression that can be easily accessed through linear simulation algorithms to estimate

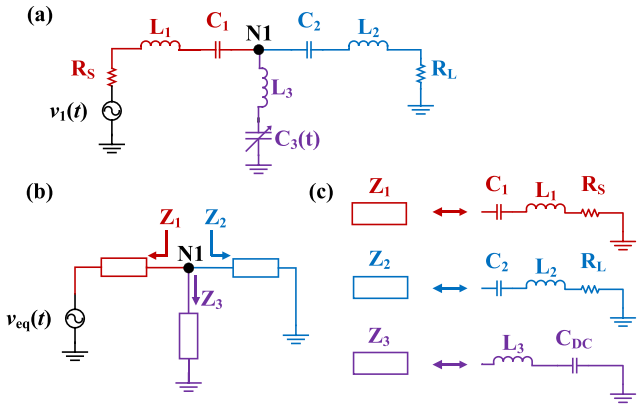

Fig. 1. (a) Initially analyzed PFD design, which is formed by three LC tanks (two static linear ones and one including a modulated varactor) and two resistors mapping the source resistance and load resistance, respectively. This PFD circuit is initially studied as a mean to extract an equivalent FD model that can be used to investigate the behavior of more general PFD designs. (b) More general PFD circuit model that includes three general impedances (Z_1–Z_3) on behalf of the LC tanks used in (a). This model is adopted in the FD analysis used in this article to analytically find P_{th}. (c) Definition of Z_1–Z_3 for the circuit shown in (a).

and minimize the P_{th}-value exhibited by any PFD that is to be designed.

A. Closed-Form Expression for P_{th}

We start our analysis from the simplified circuit shown in Fig. 1(a). After selecting as state variables the charge $q_1(t)$, $q_2(t)$, and $q_3(t)$ in the capacitors C_1–$C_3(t)$, respectively, we write the system of Kirchhoff's equations (1) that describes the circuit behavior, when assuming zero prestored electrical energy in all circuit components. R_S and R_L represent the source and load impedances and $v_1(t)$ is a continuous-wave input signal with magnitude equal to V_1

$$\begin{aligned} v_1(t) &= \frac{q_1(t)}{C_1} + \frac{q_2(t)}{C_2} + R_S q_1'(t) + R_L q_2'(t) \\ &\quad + L_1 q_1''(t) + L_2 q_2''(t) \\ v_1(t) &= \frac{q_1(t)}{C_1} + \frac{q_3(t)}{C_3(t)} + R_S q_1'(t) + L_1 q_1''(t) + L_3 q_3''(t) \\ q_1(t) &- q_2(t) - q_3(t) = 0. \end{aligned} \tag{1}$$

In (1), $C_3(t)$ can be replaced with its Taylor expansion (2), computed around its average dc value (C_{dc}).

$$C_3(t) = C_{\text{dc}}\left(1 + \epsilon\frac{C_d q_3(t)}{C_{\text{dc}}} + \epsilon^2\frac{C_{d2} q_3(t)^2}{C_{\text{dc}}^2} + \cdots\right). \tag{2}$$

In (2), ϵ represents an arbitrarily small real parameter that is used to control the perturbation order [38], [39] adopted at different stages of our analytical treatment. Also, the coefficients C_d and C_{d2} represent the first- and second-order coefficients relative to the varactor $C(v)$ characteristics, for the chosen biasing voltage (V_{dc}). Note that (2) can be used to describe the $C(v)$ characteristics of any varactor technologies, including the dc-biased transistor-based ones often preferred when designing tunable integrated circuits. When targeting the computation of P_{th}, (2) can be truncated after its first-order perturbation term [13], [16] and (1) can be simplified as

$$\begin{aligned} v_1(t) &= \frac{q_1(t)}{C_1} + \frac{q_2(t)}{C_2} + R_S q_1'(t) + R_L q_2'(t) \\ &\quad + L_1 q_1''(t) + L_2 q_2''(t) \\ v_1(t) &= \frac{q_1(t)}{C_1} + \frac{q_3(t)}{C_{\text{dc}}} - \frac{C_d \epsilon q_3(t)^2}{C_{\text{dc}}^2} + R_S q_1'(t) \\ &\quad + L_1 q_2''(t) + L_3 q_3''(t) \\ q_1(t) &- q_2(t) - q_3(t) = 0. \end{aligned} \tag{3}$$

It is convenient to transform (3) to its equivalent FD representation. However, in order to do so, it is necessary to make proper assumptions about the spectral characteristics of $q_1(t)$, $q_2(t)$, and $q_3(t)$. Here, these three charge distributions [labeled together as $q_{1,2,3}(t)$] are assumed to be formed by the superposition of two continuous-wave signals [$q^p_{1,2,3}(t)$ and $q^o_{1,2,3}(t)$], respectively, characterized by a frequency (f) equal to the generator frequency (f_{pump}) and to its divided-by-two value (f_{out}). Although the $q^o_{1,2,3}(t)$ signals are not originated from any excitation source in the circuit, assuming their existence is crucial to introduce the small perturbative components at f_{out} that enable the detection of P_{th}. Furthermore, even though the mutual relationship between $q_1(t)$, $q_2(t)$, and $q_3(t)$ is determined by the circuit dynamics, the phase lag between $q_i^p(t)$ and $q_i^o(t)$ for any arbitrarily chosen one of these signals [$q_i(t)$] can be strategically selected to lower the complexity of our following FD analysis. In this case, it is convenient to assume $q_3^o(t)$ to be in phase with $q_3^p(t)$ so that the Fourier transform of $q_3^2(t)$ in (3) only produces real components. We report in (4) the assumed distributions for $q_1(t)$, $q_2(t)$ and $q_3(t)$

$$\begin{aligned} q_1(t) &= a_1\cos(\omega_p t + \phi_1^p) + b_1\cos(\omega_o t + \phi_1^o) \\ q_2(t) &= a_2\cos(\omega_p t + \phi_2^p) + b_2\cos(\omega_o t + \phi_2^o) \\ q_3(t) &= a_3\cos(\omega_p t) + b_3\cos(\omega_o t). \end{aligned} \tag{4}$$

In (4), $a_{1,2,3}(t)$, $b_{1,2,3}(t)$, $\phi^p_{1,2}$, and $\phi^o_{1,2}$ represent the magnitude of $q^p_{1,2,3}(t)$ and $q^o_{1,2,3}(t)$ and the phase of $q^p_{1,2}(t)$ and $q^o_{1,2}(t)$, respectively. Also, ω_o and ω_p are, respectively, equal to $2\pi f_{\text{out}}$ and $2\pi f_{\text{pump}}$. Given the assumed charge distributions and starting from (3), an equivalent unilateral HB problem can be defined as in the following equation:

$$\begin{aligned} \frac{V_1}{2} &= \frac{Q_1^p + Q_1^o}{C_1} + \frac{Q_2^p + Q_2^o}{C_2} + i R_S\left(Q_1^o\omega_o + Q_1^p\omega_p\right) \\ &\quad + i R_L\left(Q_2^o\omega_o + Q_2^p\right)\omega_p - L_1\left(Q_1^o{\omega_o}^2 + Q_1^p{\omega_p}^2\right) \\ &\quad - L_2\left(Q_2^o{\omega_o}^2 + Q_2^p{\omega_p}^2\right) \\ \frac{V_1}{2} &= \frac{Q_1^o + Q_1^p}{C_1} + \frac{Q_3^o + Q_3^p}{C_{\text{dc}}} - \frac{\epsilon C_d Q_3^o\left(Q_3^o + 2Q_3^p\right)}{2C_{\text{dc}}^2} \\ &\quad + i R_S\left(Q_1^o\omega_o + Q_1^p\omega_p\right) - L_1\left(Q_1^o{\omega_o}^2 + Q_1^p{\omega_p}^2\right) \\ &\quad - L_3\left(Q_3^o{\omega_o}^2 + Q_3^p{\omega_p}^2\right) \\ Q_1^o &+ Q_1^p - Q_2^o - Q_2^p - Q_3^o - Q_3^p = 0. \end{aligned} \tag{5}$$

In (5), Q_1^p, Q_2^p, Q_3^p, Q_1^o, Q_2^o, and Q_3^o represent the single-sided FD components relative to $q_1(t)$, $q_2(t)$, and $q_3(t)$ for both f_{pump} and f_{out}. For clarity, their definition is reported in the

following equation:

$$\begin{aligned} Q_{1,2}^{p} &= \frac{1}{2}a_{1,2}e^{-i\phi_{1,2}^{p}}\delta(f-f_{\text{pump}}) \\ Q_{1,2}^{o} &= \frac{1}{2}b_{1,2}e^{-i\phi_{1,2}^{o}}\delta(f-f_{\text{out}}) \\ Q_{3}^{p} &= \frac{1}{2}a_{3}\delta(f-f_{\text{pump}}) \\ Q_{3}^{o} &= \frac{1}{2}b_{3}\delta(f-f_{\text{out}}). \end{aligned} \tag{6}$$

Also, the terms Q_3^{o2} and $Q_3^o Q_3^p$ originate from the unilateral Fourier transform of $q_3(t)^2$ when considering only the components at f_{out} and f_{pump}, their definition is reported in the following equation:

$$\begin{aligned} Q_{3}^{o2} &= \frac{1}{4}b_{3}^{2}\delta(f-f_{\text{pump}}) \\ Q_{3}^{p}Q_{3}^{o} &= \frac{1}{4}a_{3}b_{3}\delta(f-f_{\text{out}}). \end{aligned} \tag{7}$$

It is important to point out that (5) contains terms at both frequencies of interest. Since the validity of (5) must be ensured at both f_{out} and f_{pump}, each equation forming it can be divided into two equations, collecting the various terms at these two frequencies. Also, since we expect b_3 to be small, below threshold, Q_3^{o2} can be neglected without altering the validity of our analytical treatment. The resulting HB system is reported in the following equation:

$$\begin{aligned} &Q_1^o\left(\frac{-1}{C_1}-iR_S\omega_o+L_1\omega_o^2\right) \\ &\quad+Q_2^o\left(\frac{-1}{C_2}-iR_L\omega_o+L_2\omega_o^2\right)=0 \\ &Q_1^o\left(\frac{-1}{C_1}-iR_S\omega_o+L_1\omega_o^2\right) \\ &\quad+Q_3^o\left(\frac{-1}{C_{\text{dc}}}+\frac{\epsilon C_d Q_3^p}{C_{\text{dc}}^2}+L_3\omega_o^2\right)=0 \\ &Q_1^o-Q_2^o-Q_3^o=0 \\ &\frac{V_1}{2}+Q_1^p\left(\frac{-1}{C_1}-iR_S\omega_p+L_1\omega_p^2\right) \\ &\quad+Q_2^p\left(\frac{-1}{C_2}-iR_L\omega_p+L_2\omega_p^2\right)=0 \\ &\frac{V_1}{2}+Q_1^p\left(\frac{-1}{C_1}-iR_S\omega_p+L_1\omega_p^2\right) \\ &\quad+Q_3^p\left(\frac{-1}{C_{\text{dc}}}+L_3\omega_p^2\right)=0 \\ &Q_1^p-Q_2^p-Q_3^p=0. \end{aligned} \tag{8}$$

From the inspection of (8), it can be observed that all Fourier coefficients (Q_1^o, Q_2^o, Q_3^o, Q_1^p, Q_2^p, and Q_3^p) multiply a complex term that includes the static equivalent impedance seen from $N1$ (see Fig. 1) toward one specific branch of the analyzed PFD. As discussed in [34], such an important feature originates from the dependence of the conversion gain of a modulated capacitor on the impedance that such a capacitor sees from its insertion point and at the different frequencies in the circuit. Consequently, (8) can be used to extract an equivalent transformed two-tone unilateral HB system for

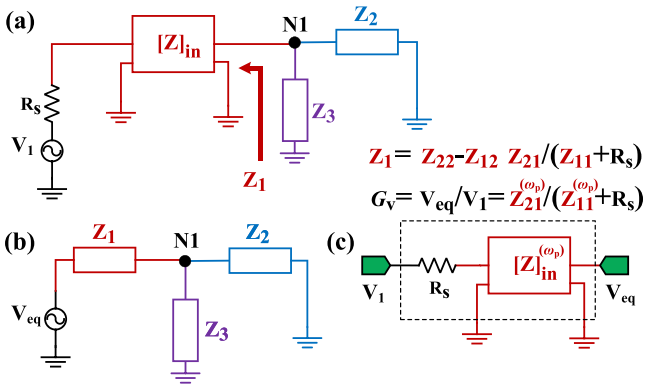

Fig. 2. (a) Schematic (at f_{pump}) of a generic PFD design with a two-port network on its input branch. (b) Schematic of the equivalent network of (a), at f_{pump}, which can be analyzed in order to find the P_{th}-value of the PFD shown in (a). As evident, this network relies on a one-port impedance (Z_1) instead of $[Z]_{\text{in}}$. Z_1 is the equivalent impedance seen by $N1$ toward the generator in (a). Furthermore, an equivalent voltage generator with magnitude V_{eq} is adopted. V_{eq} corresponds to the open-circuit voltage at f_{pump} across the output terminals of $[Z]_{\text{in}}$ in the PFD shown in (a). (c) Schematic of the network to consider when extracting G_v to find V_{eq} from V_1 or vice versa.

PFDs exhibiting different and generically complex equivalent impedances [Z_1–Z_3; see Fig. 1(b) and (c)]. In the following analysis, the value of these impedances at f_{out} and f_{pump} will be indicated as $Z_1^{(\omega_o)}$, $Z_2^{(\omega_o)}$, $Z_3^{(\omega_o)}$, $Z_1^{(\omega_p)}$, $Z_2^{(\omega_p)}$, and $Z_3^{(\omega_p)}$. In order to derive the transformed HB system, two important aspects must be considered. First, Z_3 must include the static impedance of the modulated varactor. Also, the voltage (V_{eq}) to use in the transformed HB system coincides with the applied input voltage (V_1) only in the typical cases in which the impedance used in the input branch of the PFD is a one-port network, connected between the input port and $N1$. In contrast, when a two-port network ($[Z]_{\text{in}}$) is used in the input branch of the PFD [see Fig. 2(a)], a different excitation voltage must be adopted [see Fig. 2(b)]. Such a voltage coincides with the equivalent open-circuit voltage component, at f_{pump}, extracted at the output port of $[Z]_{\text{in}}$. Also, its value can be found as $G_v V_1$, where G_v is the open-circuit voltage gain at f_{pump} of the equivalent two-port network formed by the series combination of R_S with $[Z]_{\text{in}}$ [see Fig. 2(c)]. The resulting transformed unilateral HB system for PFDs using generic Z_1–Z_3 is reported in the following equations:

$$\begin{aligned} -iQ_1^oZ_1^{(\omega_o)}\omega_o-iQ_2^oZ_2^{(\omega_o)}\omega_o &= 0 \\ -iQ_1^oZ_1^{(\omega_o)}\omega_o-iQ_3^oZ_3^{(\omega_o)}\omega_o+\frac{\epsilon C_d Q_3^pQ_3^o}{C_{\text{dc}}^2} &= 0 \\ Q_1^o-Q_2^o-Q_3^o &= 0 \\ \frac{V_{\text{eq}}}{2}-iQ_1^pZ_1^{(\omega_p)}\omega_p-iQ_2^pZ_2^{(\omega_p)}\omega_p &= 0 \\ \frac{V_{\text{eq}}}{2}-iQ_1^pZ_1^{(\omega_p)}\omega_p-iQ_3^pZ_3^{(\omega_p)}\omega_p &= 0 \\ Q_1^p-Q_2^p-Q_3^p &= 0. \end{aligned} \tag{9, 10}$$

In the following, in favor of a more compact analytical treatment, we limit our analysis to the common case in which PFDs use one-port networks in their input branch ($G_v = 1$).

The system in (10) is then solved in terms of Q_1^p, Q_2^p, and Q_3^p, when assuming $V_{\rm eq}$ equal to V_1 [see (11)]. It is important to point out that Q_1^p, Q_2^p, and Q_3^p are the only components setting the large-signal periodic behavior of PFDs

$$Q_1^p = \frac{-iV_1\left(Z_2^{(\omega_p)} + Z_3^{(\omega_p)}\right)}{4Z_{\rm eq}^{(\omega_p)}\omega_o}$$
$$Q_2^p = \frac{-iV_1 Z_3^{(\omega_p)}}{4Z_{\rm eq}^{(\omega_p)}\omega_o}$$
$$Q_3^p = \frac{-iV_1 Z_2^{(\omega_p)}}{4Z_{\rm eq}^{(\omega_p)}\omega_o}. \tag{11}$$

In (11), $Z_{\rm eq}^{(\omega_p)}$ is defined as

$$Z_{\rm eq}^{(\omega_p)} = Z_2^{(\omega_p)}Z_3^{(\omega_p)} + Z_1^{(\omega_p)}\left(Z_2^{(\omega_p)} + Z_3^{(\omega_p)}\right). \tag{12}$$

Similarly, it is possible to compute Q_1^o, Q_2^o, and Q_3^o from (9), after replacing Q_3^p with the expression reported in (11). It is useful to rewrite the resulting set of equations in a matrix representation as follows:

$$\left[A\right]\begin{bmatrix} Q_1^o \\ Q_2^o \\ Q_3^o \end{bmatrix} = 0 \tag{13}$$

where [A] is defined as

$$\begin{bmatrix} -iZ_1^{(\omega_o)}\omega_o & -iZ_2^{(\omega_o)}\omega_o & 0 \\ -iZ_1^{(\omega_o)}\omega_o & 0 & -iZ_3^{(\omega_o)}\omega_o - \dfrac{iV_1\epsilon C_d Z_2^{(\omega_p)}}{4{C_{\rm dc}}^2 Z_{\rm eq}^{(\omega_p)}\omega_o} \\ 1 & -1 & -1 \end{bmatrix}. \tag{14}$$

The matrix shown in (14) can be used to identify the minimum input voltage magnitude $V_{\rm th}$ activating the desired subharmonic oscillation. In order to do so, it suffices to find the V_1-value that nulls the determinant of the system matrix shown in (14). The expressions of the so found $V_{\rm th}$-value, as well as the corresponding $P_{\rm th}$-value, are reported in the following equations:

$$V_{\rm th} = \frac{-4C_{\rm dc}^2 Z_{\rm eq}^{(\omega_o)} Z_{\rm eq}^{(\omega_p)}\omega_o^2}{\epsilon C_d\left(Z_1^{(\omega_o)} + Z_2^{(\omega_o)}\right)Z_2^{(\omega_p)}} \tag{15}$$

$$P_{\rm th} = \frac{|V_{\rm th}|^2}{8R_S}. \tag{16}$$

In (15) and (16), $Z_{\rm eq}^{(\omega_o)}$ is defined as

$$Z_{\rm eq}^{(\omega_o)} = Z_2^{(\omega_o)}Z_3^{(\omega_o)} + Z_1^{(\omega_o)}\left(Z_2^{(\omega_o)} + Z_3^{(\omega_o)}\right). \tag{17}$$

As evident from (15) and (16), $V_{\rm th}$ and $P_{\rm th}$ are explicit functions of all the impedance values characterizing the operation of PFDs at both $f_{\rm out}$ and $f_{\rm pump}$. Such impedances significantly shape the stability region of PFDs, thus playing a critical role in their design and performance characteristics. In particular, the inspection of (15) permits the establishment of a general guideline for the design of PFDs. First, (15) clearly shows that low-capacitance varactors (low $C_{\rm dc}$), with a wide tuning range (large C_d), are generally desirable to minimize $V_{\rm th}$. In addition, (15) shows that a quadratic increase of $V_{\rm th}$ is expected at increasing ω_o-values. Such an important feature is mainly due to the increasing challenge of achieving large voltage swings, across variable capacitors, at higher driving frequencies. Ultimately, (15) provides an essential guidance in the synthesis of Z_1–Z_3. In fact, this synthesis can be tackled through conventional linear methods targeting the minimization of (15), even for complex high-frequency board designs that are generally sensitive to undesired parasitics. The ability to design Z_1–Z_3 through conventional linear synthesis approaches is essential to enable optimum and reliable performance. Therefore, it is straightforward to verify that the minimum $P_{\rm th}$ can be attained when four resonant conditions are satisfied. These conditions suggest that the following holds.

1) The series of Z_2 and Z_3 has to be designed to series resonate at $f_{\rm out}$ (i.e., $Z_2^{(\omega_o)} + Z_3^{(\omega_o)} \rightarrow {\rm Re}\{Z_2^{(\omega_o)}\} = R_L'$).
2) The series of Z_1 and Z_3 has to be designed to series resonate at $f_{\rm pump}$ (i.e., $Z_1^{(\omega_p)} + Z_3^{(\omega_p)} \rightarrow {\rm Re}\{Z_1^{(\omega_p)}\} = R_S'$).
3) Z_1 has to be designed to parallel resonate at $f_{\rm out}$ (i.e., $Z_1^{(\omega_o)} \rightarrow \infty$).
4) Z_2 has to be designed to parallel resonate at $f_{\rm pump}$ (i.e., $Z_2^{(\omega_p)} \rightarrow \infty$).

In the listed conditions, R_S' and R_L' represent the equivalent resistances observed from $N1$ when looking toward the source and the load, respectively. Even when assuming all components to be lossless, R_S' and R_L' can be different from R_S and R_L. For instance, their value can be made strategically lower through the adoption of impedance transformation stages, as will be discussed in Section III. Therefore, when Z_1– Z_3 are optimally designed, $V_{\rm th}$ becomes

$$V_{\rm th}^{\rm min} = \frac{4C_{\rm dc}^2 R_L' R_S'\omega_o^2}{\epsilon C_d}. \tag{18}$$

When the use of a minimum number of lumped components is needed in favor of the highest degree of miniaturization, the optimum synthesis of Z_1–Z_3 can be tackled through the strategic use of five electrical components (C_1, C_2, L_1, L_2, and L_3). In particular, the following holds.

1) Z_1 can be realized as the parallel combination of an inductor (L_1) and a capacitor (C_1), whose resonance frequency matches the output frequency at which the minimum $P_{\rm th}$ is desired.
2) Z_2 can be realized as the parallel combination of an inductor (L_2) and a capacitor (C_2), whose resonance frequency is equivalent to twice the output frequency at which the minimum $P_{\rm th}$ is desired.
3) Z_3 includes the static portion ($C_{\rm dc}$) of the varactor electrical characteristics; it can be realized by adding an inductor (L_3) whose value is directly related to both $Z_2^{(\omega_o)}$ and $Z_1^{(\omega_p)}$.

It is important to note that, by satisfying the four resonant conditions, it is possible to prevent any undesired reduction of the voltage swing across the varactor due to the current at $f_{\rm pump}$ leaking through the output branch. Furthermore, any leakage of the generated power at $f_{\rm out}$ into the input source circuitry is prevented. Also, note that $P_{\rm th}$ is a function of all the abovementioned circuit components. Among them,

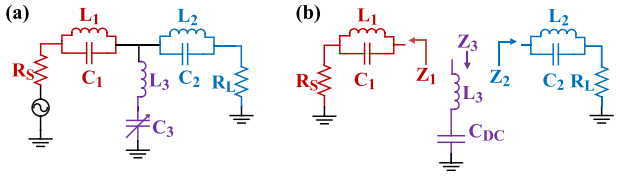

Fig. 3. (a) Schematic of the 200:100 -MHz PFD used as a case study in this article. The values of the adopted circuit components are: $L_1 = 382.5$ nH, $L_2 = 742.5$ nH, $C_1 = 6.6$ pF, $C_2 = 0.85$ pF, $L_3 = 500$ nH, $C_{dc} = 1.7$ pF, $C_d = -0.3$, and $C_{d2} = 0.02$. (b) Schematic of Z_1–Z_3 for the same PFD.

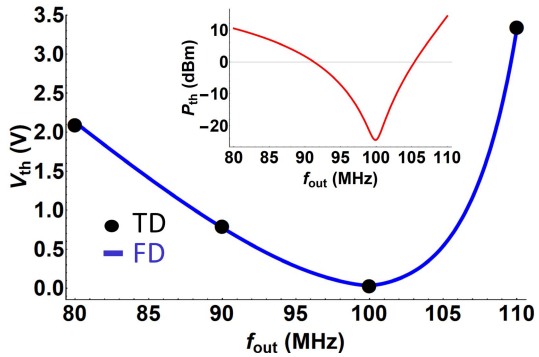

Fig. 4. Black dot: V_{th} values versus f_{out} numerically determined through TD methods applied to the PFD shown in Fig. 3. Blue line: analytically calculated V_{th} values [see (15)] for the same PFD. Red line: P_{th} distribution corresponding to the V_{th} one plotted in blue.

C_{dc} depends on the available varactor technology, whereas L_1, C_1, L_2, and C_2 depend heavily on the chosen value of L_3. Consequently, it is convenient to search for the optimal values of L_1, C_1, L_2, and C_2 that satisfy the listed resonant conditions in terms of C_{dc} and L_3 in the following equation:

$$C_1 = \frac{4C_{dc}}{3\left(-1+16L_3C_{dc}f_{out}^2\pi^2\right)}$$
$$C_2 = -\frac{C_{dc}}{3\left(-1+4L_3C_{dc}f_{out}^2\pi^2\right)}$$
$$L_1 = \frac{3\left(-1+16L_3C_{dc}f_{out}^2\pi^2\right)}{16C_{dc}f_{out}^2\pi^2}$$
$$L_2 = -\frac{3\left(-1+4L_3C_{dc}f_{out}^2\pi^2\right)}{16C_{dc}f_{out}^2\pi^2}. \quad (19)$$

Despite the fact that a low C_{dc} value would be required to ensure the minimum P_{th}, the use of ultralow-capacitance varactors is not practical as it often leads to suboptimal performance. This important feature is mostly determined by the limited Q of available inductors. This limitation constrains L_1–L_3 not to exceed certain values, in order to prevent undesired and significant increases of R'_L and R'_S. As a case study, it is now instructive to extract V_{th} through (15) for a generic simplified PFD-design, formed by lossless inductors and capacitors. The resulting value can then be compared with the one numerically found through TD-based methods, in order to confirm the validity of the reported analytical approach. The chosen device, a 200:100-MHz PFD, as well as the adopted L_3, C_{dc}, C_d, and C_{d2} values, along with the corresponding optimal L_1, L_2, C_1, and C_2 values, are reported in Fig. 3.

The estimated V_{th} values based on (15) are shown in Fig. 4, together with some corresponding results for different values

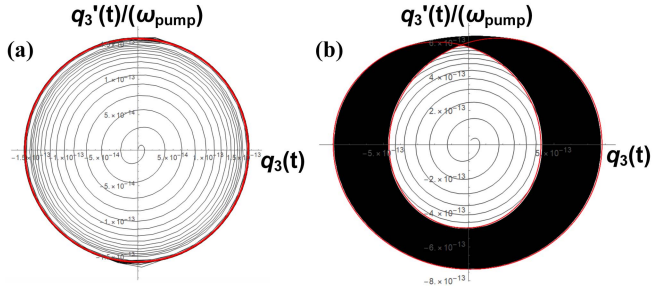

Fig. 5. (a) Phase portrait of the charge $[q_3(t)]$ in the varactor of the analyzed PFD (see Fig. 3), for $V_1 = 0.037$ V (thus below V_{th}). This plot was computed by assuming the varactor to be completely discharged at the moment ($t = 0$) in which the input voltage is applied to the circuit. In red, the typical limit cycle describing the dynamical behavior of the analyzed PFD after reaching its steady-state periodic characteristics is also reported. (b) Phase portrait of $q_3(t)$ for $V_1 = 0.039$ V (thus above V_{th}). This plot was computed by assuming the varactor to be completely discharged at the moment ($t = 0$) in which the input voltage is applied to the circuit. After a limited number of excitation cycles, the portrait exhibits a period that is twice the excitation period. Consequently, once the PFD reaches its steady-state periodical regime, the trajectory described by the system (see the red line) assumes a different shape from conventional limit cycles.

of f_{out}-values (keeping $f_{pump} = 2f_{out}$), obtained through TD methods. Clearly, the V_{th} values derived through numerical TD methods match very closely the analytically predicted ones, thus demonstrating the validity of our analytical findings. The P_{th} values corresponding to the V_{th} values found through (15) are also shown in Fig. 4. As is evident, when neglecting the ohmic losses introduced by each adopted element and when properly selecting the different components forming its network, the investigated PFD can exhibit a P_{th} value (for $f_{out} = 100$ MHz) that is lower than -24 dBm, corresponding to V_{th} of 0.038 V. To further verify the substantial and desired change in the dynamical behavior of the analyzed PFD, for V_1 being slightly higher or slightly lower than V_{th}, we report the phase portraits [40] (see Fig. 5) relative to $q_3(t)$ and derived through TD methods, when assuming that f_{out} equals 100 MHz (i.e. f_{pump} equals 200 MHz) and for V_1 equal to 0.037 and 0.039 V, respectively. As is evident, substantially different behaviors characterize the operation of the analyzed PFD for the two investigated V_1 values. In particular, for V_1 equal to 0.037 V, the portrait of $q_3(t)$ shows the existence of a limit cycle. This cycle maps the evolution of $q_3(t)$ and $q'_3(t)$ as time evolves from the origin of the reference system ($t = 0$) and zero prestored charge exists in the different capacitors. In contrast, for V_1 equal to 0.039 V (thus being higher than the expected V_{th} value), the portrait exhibits a substantially different behavior. In fact, once the PFD reaches its steady-state periodic operational regime (see the red lines in Fig. 5), the portrait exhibits twice the period that exhibits in the former case. Such a unique feature maps (in the TD) the origin of a period-doubling mechanism that marks the existence of a subharmonic oscillation in the circuit. The phenomenon of period doubling can also be directly observed by extracting the Poincaré map (PM) [41] (see Fig. 6). This tracks the radius of the limit cycle of $q_3(t)$($r = ((q_3(t+nT_s)^2 + ((q'_3(t+nT))/\omega_p)^2)^{1/2}$, where n is an integer number) versus V_1, for consecutive returns (incre-

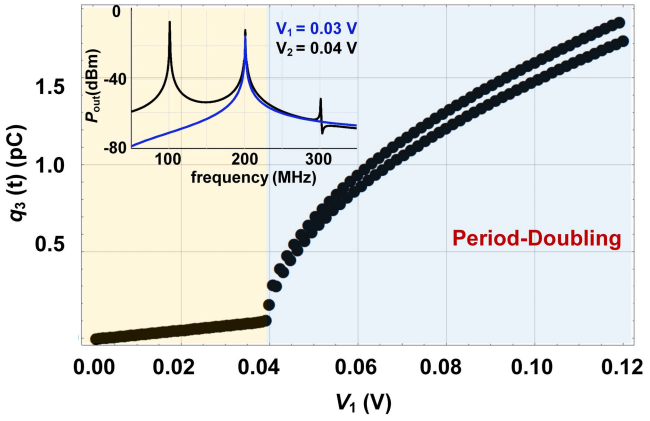

Fig. 6. PM relative to the charge $q_3(t)$ versus V_1 for the PFD shown in Fig. 3. As is evident, for V_1-values that exceed the same V_{th}-value that was analytically found through (15), the analyzed PFD undergoes a change in its dynamical characteristics that results in the activation of a period-doubling mechanism. In the inset, the spectrum of the output power for the same PFD shown in Fig. 3 is reported for V_1-values that are right below and above V_{th}.

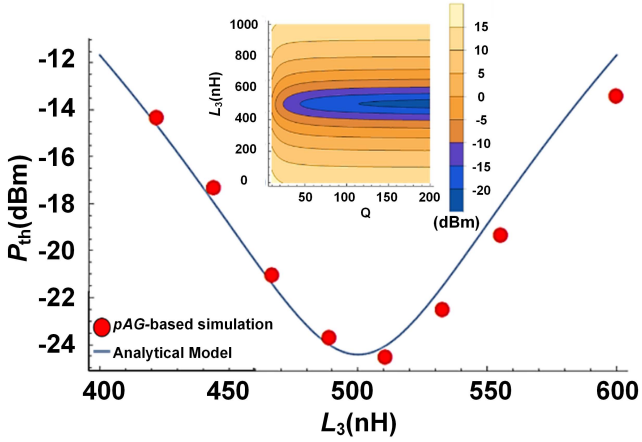

Fig. 7. Analytically found trend (blue line) of P_{th} versus L_3 and simulated P_{th} values through the pAG technique (red dots), for a limited set of L_3-values relative to the PFD described in Fig. 3. It is important to point out that the HB simulator adopted to estimate P_{th} through the pAG technique has been configured to include 25 harmonics of f_{out}, in favor of a more accurate prediction of the PFD response above the threshold. In the inset, a contour plot is reported, simultaneously mapping the impact on P_{th} of L_3 and the quality factor (Q), which is considered to be the same for all the inductors used in Fig. 3.

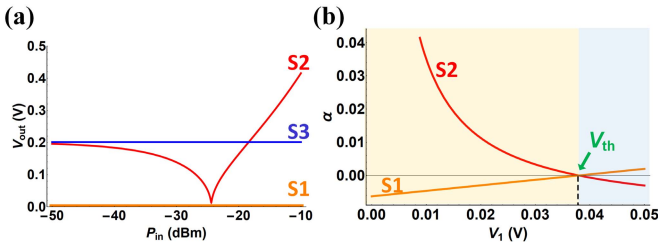

Fig. 8. (a) Solution amplitudes of the possible numerically found voltage (V_{out}) components (at f_{out}) across the load resistance R_L of the PFD shown in Fig. 3. Note that three different V_{out} distributions (relating to the solution sets S1–S3) are possible. (b) Real part of the eigenvalue (α) of [J] for S1 and S2. The α value of S3 is constant and positive for all V_1-values, thus being a clear indication that S3 is not a stable solution for the system. For this reason, its distribution with respect to V_1 has not been included here.

mental n-values) on the map. This can be done by sampling the dynamical steady-state large-signal TD response of the analyzed PFD with a sampling rate that is equal to the excitation frequency while assuming a continuously increasing driving voltage. As shown in Fig. 6, for $V_1 < V_{th}$, the PM shows a continuous trend with respect to V_1. Such a unique feature is a clear indication that $q_3(t)$ has a period that is equal to $1/f_{pump}$. In contrast, for $V_1 \geq V_{th}$, the PM exhibits two separate lines. The existence of two consecutive lines in PMs is a clear indication of the different q_3 values that the system exhibits (above threshold) at the end of consecutive sampling periods. This dynamical feature is also used often to numerically identify, through TD methods, the presence of period-doubling regimes in nonlinear dynamical systems. Instead, in order to confirm that the analytically derived P_{th} values closely match the ones found with a commercial circuit simulator through the pAG technique (see Section II), we compared the distributions of P_{th} versus L_3 extracted, both analytically and through the application of the pAG technique, for the circuit in Fig. 3. As can be observed from Fig. 7, the distribution of P_{th} versus L_3, derived through the pAG technique, agrees with the one analytically calculated using (16). This further demonstrates the validity of our analytical findings. It is worth mentioning that in order to extract the simulated data points shown in Fig. 7 (see the red points), a P_{in}-sweep of 6000 steps had to be configured for the HB simulator to converge to the desired nontrivial solution. This constraint can lead to design times, for optimized high-frequency PFDs, which can exceed days. Ultimately, we analytically studied the dependence of P_{th} on the Q value that can be exhibited by practical inductors forming the circuit shown in Fig. 3 (see the inset in Fig. 7). For simplicity, in order to do so, we assumed that all the inductors were exhibiting the same Q. Interestingly, our investigation revealed that ultralow P_{th}-values can indeed be attained, even when using inductors with Q-values that are only around 50.

B. Evaluating the Response of PFDs for $P_{in} > P_{th}$

In Section II-A, a closed-form expression was found to evaluate the threshold voltage and power (V_{th} and P_{th}) activating a 2:1 subharmonic oscillation in varactor-based PFDs. In this section, the procedure to analytically estimate the complete response of PFDs, below and above the parametric threshold, is discussed and applied to the PFD circuit shown in Fig. 3. The assessment of the PFD response, after the occurrence of a bifurcation, requires solving the systems in (1) and (2) without neglecting any second-order perturbation term proportional to ϵ^2. This increased complexity renders the solution of these systems only computable through numerical methods. However, some important features can still be identified. In fact, three sets of Q_1^o, Q_2^o, and Q_3^o are found to be potential solutions for the new HB system that includes the higher order terms. One set (S1) is representative of the trivial solution ($Q_1^o = Q_2^o = Q_3^o = 0$), thus describing the evolution of the PFD when no input signal at f_{out} exists in the circuit and when assuming $V_1 \ll V_{th}$. Another set (S3) shows the quasi-uniform and not-nulled distributions for Q_1^o, Q_2^o, and Q_3^o versus the magnitude of V_1. Finally, the last solution set (S2) corresponds to more complex distributions for Q_1^o, Q_2^o, and Q_3^o versus the magnitude of V_1, exhibiting nulled

values for V_1 approaching V_{th}. The amplitudes of the voltage components across R_L (V_{out}), at f_{out}, for solutions S1–S3 were analytically determined and plotted versus the input power (P_{in}) at f_{pump}, for the investigated PFD shown in Fig. 3. Fig. 8 shows the extracted trends of V_{out} versus P_{in} for S1–S3. Due to the existence of three possible steady-state periodic solutions (S1–S3), the complete response of the analyzed PFD can only be determined analytically by evaluating the stability of each solution while varying the magnitude of the applied input signal. In order to do so, matrix A in (14), now including the higher order terms, can be linearized around each solution in order to evaluate the evolution of the system in the presence of small perturbations acting on the steady-state amplitudes of Q_1^o, Q_2^o, and Q_3^o relative to the same solution. It is worth pointing out that the resulting linearized matrix represents a Jacobian matrix ([J]) that provides the means to investigate the stability of any possible solution at f_{out}. This can be done by looking at the sign of the purely real eigenvalue (λ) of [J] (see Fig. 8). In particular, by looking at the real part (α) of λ, it is straightforward to realize that S3, for the PFD shown in Fig. 3, corresponds to a positive and constant α-value for any V_1-value, thus representing an unstable fixed point for the system. In contrast, for both S1 and S2, the sign of α changes when V_1 approaches V_{th}. In particular, S1 represents the only stable solution for $V_1 < V_{th}$, whereas S2 represents the only stable solution for $V_1 \geq V_{th}$. In other words, the trivial solution is stable for $V_1 < V_{th}$, whereas the dividing solution is stable for $V_1 \geq V_{th}$. It is also worth pointing out the fact that S1 and S2 flip their stability at the same V_1-value, which suggests that the rising of the subharmonic oscillation occurs through a supercritical bifurcation. For this reason, no abrupt jump is expected in the PFD frequency response, as its operation involves the transition from one operational regime to the other. As evident, the V_{th} value extracted from Fig. 8 matches the one we found through both the observation of the phase portraits (see Fig. 5), the analysis of the PM (see Fig. 6), and the use of the pAG technique with a commercial HB simulator (see Fig. 7). After determining the stability of S1 and S2, it is easy to estimate the output power of the PFD in Fig. 3 when this is driven at $f_{pump} = 200$ MHz and when P_{in} is progressively increased to activate the division process in the circuit. In Fig. 9, we report the PFD output power (P_{out}, delivered to R_L) versus P_{in} for the PFD shown in Fig. 3.

III. Lumped Realization of a 200:100-MHz PFD

In Section III, a closed-form expression for P_{th} was derived. In order to experimentally verify the validity of our findings, we designed a 200:100-MHz PFD using lumped components available on the shelf. The PFD was assembled on a PCB made of FR4 and its performance was characterized using conventional RF measurement equipment. A detailed description of the adopted design flow, as well as the analysis of our measured results, is discussed in the remainder of this section.

A. Design of a 200:100-MHz PFD

The design of the reported PFD targeted the minimization of P_{th} at a chosen f_{out} value of interest. In this case, 100 MHz

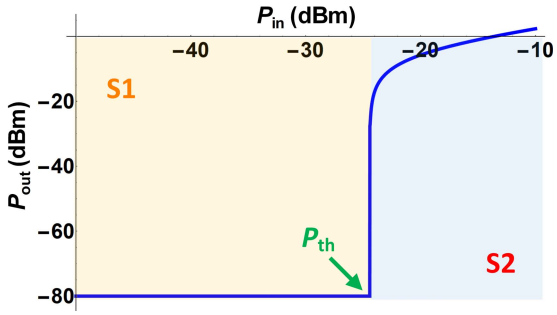

Fig. 9. Numerically extracted output power (P_{out}) for the PFD shown in Fig. 3. The plot was generated with the assumption of a white noise power spectral density in the circuit, resulting in −80 dBm of power for $P_{in} < P_{th}$ (when the trivial solution is the only stable one for the circuit).

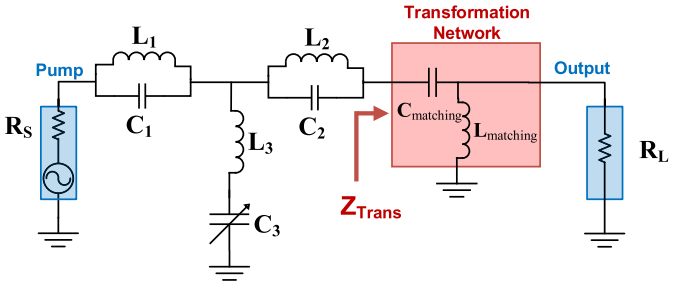

Fig. 10. Schematic of the PFD we built in this article. The circuit is designed to be driven by a 50-Ω generator and to be attached (at its output) to a 50-Ω output load (R_L).

was chosen as the desired output frequency. Fig. 10 shows a schematic of the PFD architecture that we selected for the experimental validation. This PFD design relies on the five components [L_1, L_2, C_1, C_2, and L_3; see (19)] used in the simplified PFD circuit in Fig. 3. However, two additional components were added: a capacitor and an inductor. These components, labeled as $C_{matching}$ and $L_{matching}$, were chosen so as to form the equivalent lumped representation of a quarter-wave transformation stage at f_{out}. It is important to point out that the adoption of this stage is key to lowering the P_{th} value that can be attained through only the use of the other five components. In fact, the use of this stage reduces the impact of the output load (R_L) on the stability of the PFD, by converting R_L to an impedance (Z_{Trans}) whose value, at f_{out}, is real and lower than 1 Ω. In other words, the use of the transformation stage permits the reduction of R'_L, thus minimizing V_{th}^{min} and, consequently, P_{th} [see (16) and (18)]. Moreover, the adoption of a transformation network relying on a series capacitor permits the use of $C_{matching}$ also as a dc blocker. It is worth mentioning that due to the adoption of the transformation stage, the varactor sees a low resistance (R'_L) at f_{out} that closely matches the one seen by each varactor in previously reported differential PFD topologies [26], [42]. However, since such a low R'_L value is attained without requiring two identical varactors (thus twice the C_{dc} value) simultaneously connected to the input source, the reported PFD can reach lower P_{th}-values than its corresponding differential counterpart. However, differential topologies inherently exhibit a large spectral purity, which can only be attained by single-ended configurations when these rely on high-order and high-Q passive networks. The

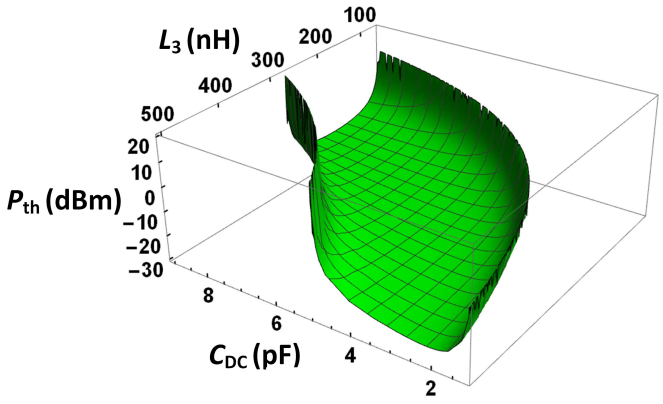

Fig. 11. 3-D plot mapping the distribution of P_{th} versus L_3 and C_{dc}, where Q equal to 50 was assumed for all the inductors in the circuit.

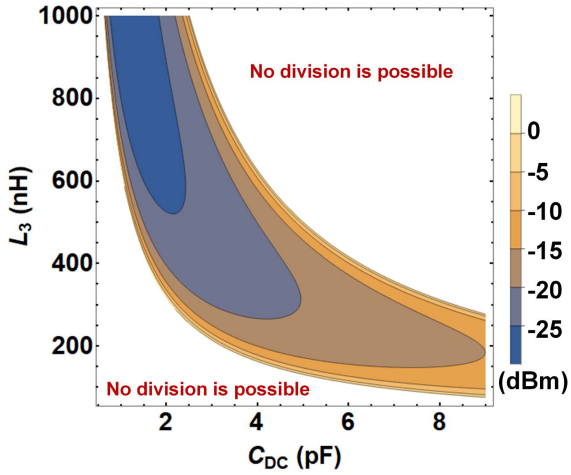

Fig. 12. Contour plot mapping P_{th} versus L_3 and C_{dc}, assuming that Q of all the inductors is 50. The range of these two parameters in which no division is possible is also identified.

selected values for $C_{matching}$ (227 pF) and $L_{matching}$ (11.3 nH) were chosen so that the lowest Z_{Trans} value could be attained when considering the typical Q values exhibited by available inductors on the shelf. It is worth mentioning that because of the more dispersive behavior of Z_2 with respect to the one of the simplified circuit in Fig. 3, the resonant conditions that must be satisfied in order to minimize P_{th} lead to different expressions for the optimal values of L_1, L_2, C_1, and C_2 versus L_3 and C_3. However, such differences are small and, consequently, practically negligible. Furthermore, the optimal component valuessignificantly depend on the maximum Q that can be exhibited by L_1 and L_2 in practice. Therefore, after finding a commercially available hyperabrupt varactor (model: Skyworks SMV1405), characterized by C_{dc} values ranging from 1 pF to 10 pF and capable of exhibiting high C_d values [see (2)], we analytically studied the distribution of P_{th} [see (16)] versus L_3 and C_{dc}. In order to do so, the C_d value exhibited by the selected varactor was expressed in terms of C_{dc}. This simplification made C_{dc} the only required varactor parameter to extract P_{th}. Moreover, the derived P_{th} distribution was found after selecting the L_1, L_2, C_1, and C_2 values that satisfy the resonant conditions discussed in Section II-A, for each analyzed set of L_3 and C_{dc} values. In Figs. 11 and 12, we report the computed trend and the contour plot of P_{th} versus L_3 and C_{dc} when assuming Q of L_1, L_2, and L_3 to be 50. This value corresponds to the best quality factor that we could find for off-the-shelf inductors that are in the same range as those required to optimally design a 200:100-MHz PFD relying on ideal lossless components to work (see Fig. 3). As is evident, a monotonically decreasing P_{th} is attained as L_3 is increased. However, the adoption of L_3 values larger than 800 nH would require C_2 to be lower than 0.5 pF. This design constraint would expose any PFD built on a PCB to the risk of exhibiting performance that are too sensitive to unmodeled variations of the actual C_2 value. Also, because of the limited availability of surface-mounted commercial inductors, simultaneously showing large inductance, high-Q values (exceeding 50), and a self-resonance frequency higher than the maximum frequency of interest (200 MHz), the use of excessively large L_3 values is also not practical. Based on these limitations, we selected the C_{dc} value (1.7 pF) that minimizes P_{th}, given the largest suitable L_3-value that we could find (500 nH). By looking at the $C(v)$ characteristic of the chosen varactor, this optimal C_{dc} value permits to easily find the corresponding dc voltage (1.6 V) that must be used in the actual PFD circuit to bias the varactor. Also, after selecting L_3, we looked at the sensitivity of the optimal C_{dc} value as we vary Q exhibited by L_1–L_3, ranging from 10 to 50. As is evident from Fig. 13, we found the optimal C_{dc} value to be only slightly dependent on Q of the adopted inductors, thus being almost immune to nonidealities that often make commercial inductors exhibit different Q values from their nominal values. In summary, the values that we selected for the experimental demonstration are 382.5 nH, 742.5 nH, 6.6 pF, 0.85 pF, and 500 nH for L_1, L_2, C_1, C_2, and L_3, respectively. Based on these values, we searched for commercial components with the closest nominal behavior to the desired ones. Then, we assembled a distributed model of the board layout using microstrip components. After building this model, we minimized the impact of the board layout on P_{th}. In order to do so, we developed an *ad hoc* design framework that allows for the extraction of the values of $Z_1^{(\omega_o)}$, $Z_2^{(\omega_o)}$, $Z_3^{(\omega_o)}$, $Z_1^{(\omega_p)}$, $Z_2^{(\omega_p)}$, and $Z_3^{(\omega_p)}$ directly from the distributed model. These values are then used and automatically updated during an optimization routine targeting the minimization of (16), which is used as the goal function. During this optimization step, we also considered the available S-parameters for the lumped components that we selected. We report, in Fig. 14 (see the green line), the analytically derived distribution of P_{th} versus f_{out}, extracted through (16) after determining the best layout geometry and under the assumption that the input frequency is always twice the f_{out} value. The same distribution was also evaluated using the pAG technique by replacing the optimized distributed model for the board with its actual electromagnetic simulated RF model (see the red points in Fig. 14). It can be seen that

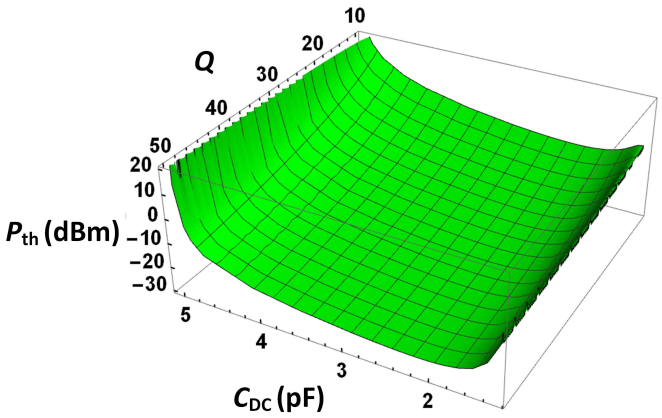

Fig. 13. 3-D plot mapping the distribution of P_{th} versus C_{dc} and Q, when assuming L_3 to be 500 nH (thus the value used in our built PFD), and all the inductors showing the same Q.

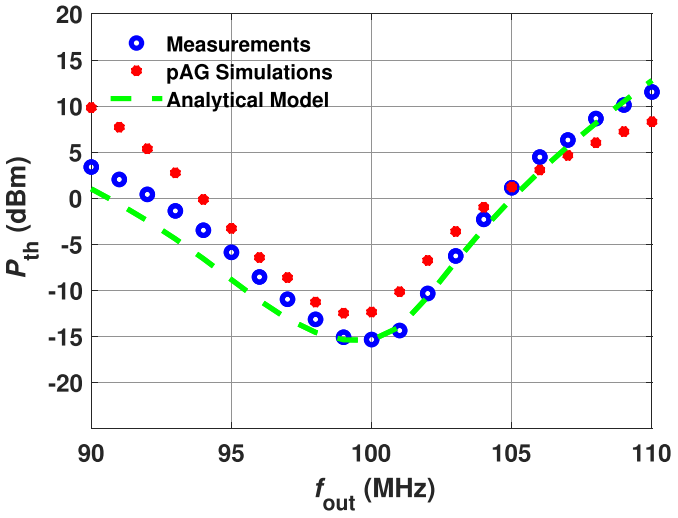

Fig. 14. Simulated distributions of P_{th} versus f_{out} for the PFD built in this article. In green, simulated values extracted through the reported analytical method once this is applied, directly in a circuit simulator, to the PFD built in this article. In red, simulated values extracted through the pAG technique. In blue, measured P_{th} values for the same frequencies considered during our simulations. In order to extract both the simulated and the measured data, f_{pump} was kept equal to $2f_{out}$ for all investigated f_{out} values.

TABLE I

COMPARISON BETWEEN THE MAIN PERFORMANCE CHARACTERISTICS OF THE PFD DEVELOPED IN THIS ARTICLE WITH PREVIOUSLY REPORTED PASSIVE PROTOTYPES, ALSO OPERATING WITHIN THE UHF RANGE

	P_{th} (dBm)	f_{out} (MHz)	Implementation
This work	-15	100	lumped
[16]	10.5	226.7	lumped
[25]	6	315	lumped
[43]	-6.5	1277	lumped
[42]	4	850	hybrid

both simulation approaches exhibit closely matching trends and predicted minimum P_{th} values lower than −12.5 dBm at f_{out} equal to 100 MHz.

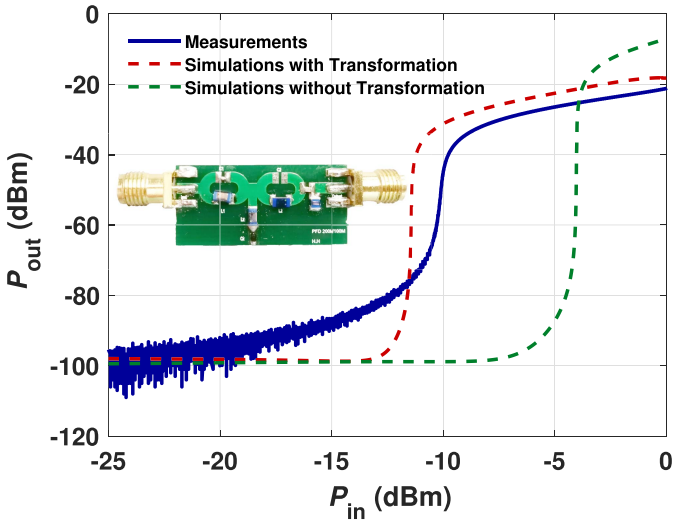

Fig. 15. Measured (blue line) and simulated (red line, using the pAG technique) distributions of P_{out} versus P_{in} for the PCB built in this article. For comparison, the simulated distribution of P_{out} versus P_{in}, without the transformation stage, is shown in green. In order to reach the highest accuracy, the HB order in our simulations was set to 25. As is evident, the measured and simulated P_{th} values (see the blue and red points, relative to f_{out} equal to 100 MHz, in Fig. 14) match closely the value we found through our analytical method applied directly during the PFD design in a commercial HB circuit simulator (see the P_{th} value, at f_{out} equal to 100 MHz, for the green line in Fig. 14). Inset: photograph of the fabricated PFD.

B. Measured Results

The designed PFD was built on a PCB made of FR4 (see the inset of Fig. 15). An external bias-T (model Inmet 8800SMF3-06) was used to simultaneously drive the PFD input port with an RF signal and with a dc voltage (1.6 V) required to bias the varactor. The output performance of the PFD, terminated on a 50-Ω resistive load, was characterized using conventional RF bench-top measurement equipment. In particular, first, we extracted the measured P_{th} values for f_{out} ranging from 90 to 110 MHz (the same range exploited during the PFD design phase; see Fig. 14). As is evident from Fig. 14, the measured P_{th} values match closely the corresponding values extracted, in a commercial circuit simulator, through our new analytical approach and through the adoption of the pAG technique. A minimum P_{th} equal to −15 dBm was measured at the targeted designed f_{out} value (100 MHz). To the best of the authors' knowledge, such a low P_{th} value is the lowest one ever reported for passive PFDs operating within the same frequency range (see Table I). Then, we extracted the PFD output power (P_{out}) at the targeted output frequency (100 MHz). In order to do so, we used two synchronized vector network analyzers (VNAs). One network analyzer (Keysight PNA N5221A) was set up to produce the pump signal at 200 MHz and to generate a slow P_{in} sweep from −25 to 0 dBm. The other VNA (Keysight ENA E5071C) was used to track the received power at 100 MHz. The measured distribution of P_{out} versus P_{in} (see Fig. 15) closely follows the predicted distribution found through the pAG technique. It is worth mentioning that a much higher P_{th} value would have been attained without the use of a transformation stage (see the simulated green trend in Fig. 15). To visualize the output response of the PFD after the activation of the division process,

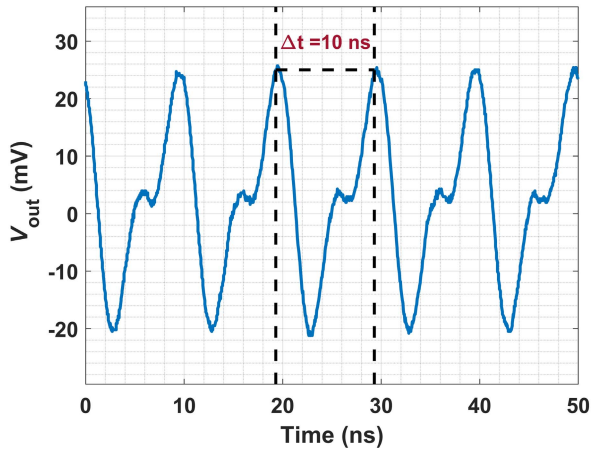

Fig. 16. Measured waveform of the output voltage of the PFD, extracted from an oscilloscope (Keysight DSOX6004A) when f_{out} was set to 100 MHz (i.e., f_{pump} = 200 MHz) and P_{in} was chosen to be −2 dBm, thus higher than P_{th}.

the measured TD waveform of its output voltage across R_L is also shown in Fig. 16, for a P_{in} value (−2 dBm) exceeding P_{th}. Under this operating condition, the presence of an output signal with a strong frequency component at 100 MHz can be easily observed.

IV. Conclusion

In this article, a new systematic synthesis approach is discussed to enable the design of varactor-based 2:1 PFDs, exhibiting ultralow-power thresholds (P_{th}). For the first time, it is analytically shown that the P_{th} value exhibited by PFDs can be expressed as a closed-form explicit function of the impedances seen by the variable capacitor, at the input frequency and at the main output frequency of operation. This unique feature permits the creation of optimum PFD designs, without relying on time-consuming and memory-intensive simulation approaches, but only through conventional design and optimization techniques that are frequently used in linear circuits. Due to the development of the reported analytical framework, we formulate new optimal design criteria for PFDs requiring ultralow P_{th} values. In order to experimentally validate our analytical findings, a 200:100-MHz PFD, relying on commercially available lumped components, was designed and assembled on a PCB. Due to its engineered design and despite the relatively low Q exhibited by its inductors, the fabricated PFD exhibited a record-low P_{th} value equal to −15 dBm. The design approach presented in this article opens exciting scenarios for the development of even other parametric components. In particular, the capability to obtain ultralow threshold PFDs will facilitate the future chip-scale development of PFILs, thus enabling their use to reduce the jitter level exhibited by available FSs in low-power RF transceivers.

References

[1] J. D. Adam, "Mitigate the interference: Nonlinear frequency selective ferrite devices," *IEEE Microw. Mag.*, vol. 15, no. 6, pp. 45–56, Sep. 2014.

[2] E. J. Naglich and A. C. Guyette, "Frequency-selective limiters utilizing contiguous-channel double multiplexer topology," *IEEE Trans. Microw. Theory Techn.*, vol. 64, no. 9, pp. 2871–2882, Sep. 2016.

[3] W. Lee and E. Afshari, "Distributed parametric resonator: A passive CMOS frequency divider," *IEEE J. Solid-State Circuits*, vol. 45, no. 9, pp. 1834–1844, Sep. 2010.

[4] N. A. Estep, D. L. Sounas, and A. Alu, "Magnetic-free, fully integrated, compact microwave circulator using angular-momentum biasing," in *IEEE Antennas Propag. Soc., AP-S Int. Symp. Dig. (APSURSI)*, Jul. 2014, pp. 340–341.

[5] M. D. Shulman, O. E. Dial, S. P. Harvey, H. Bluhm, V. Umansky, and A. Yacoby, "Demonstration of entanglement of electrostatically coupled singlet-triplet qubits," *Science*, vol. 336, no. 6078, pp. 202–205, Apr. 2012.

[6] I. Kovacic and M. J. Brennan, *The Duffing Equation: Nonlinear Oscillators and their Behaviour*. Hoboken, NJ, USA: Wiley, 2011.

[7] A. Collado and A. Georgiadis, "Improving wireless power transmission efficiency using chaotic waveforms," in *IEEE MTT-S Int. Microw. Symp. Dig.*, Jun. 2012, pp. 1–3.

[8] J. Li, H. Lee, T. Chen, and K. J. Vahala, "Low-pump-power, low-phase-noise, and microwave to millimeter-wave repetition rate operation in microcombs," *Phys. Rev. Lett.*, vol. 109, no. 23, pp. 1–5, Dec. 2012.

[9] E. Kenig *et al.*, "Passive phase noise cancellation scheme," *Phys. Rev. Lett.*, vol. 108, no. 26, pp. 2–6, Jun. 2012.

[10] P. Ward and A. Duwel, "Oscillator phase noise: Systematic construction of an analytical model encompassing nonlinearity," *IEEE Trans. Ultrason., Ferroelectr., Freq. Control*, vol. 58, no. 1, pp. 195–205, Jan. 2011.

[11] A. B. Ustinov, A. V. Drozdovskii, and B. A. Kalinikos, "Multifunctional nonlinear magnonic devices for microwave signal processing," *Appl. Phys. Lett.*, vol. 96, no. 14, pp. 2008–2011, 2010.

[12] S. Ver Hoeye, F. Ramírez, and A. Suárez, "Nonlinear optimization tools for the design of high-efficiency microwave oscillators," *IEEE Microw. Wireless Compon. Lett.*, vol. 14, no. 5, pp. 189–191, May 2004.

[13] L. G. Villanueva, R. B. Karabalin, M. H. Matheny, E. Kenig, M. C. Cross, and M. L. Roukes, "A nanoscale parametric feedback oscillator," *Nano Lett.*, vol. 11, no. 11, pp. 5054–5059, Nov. 2011.

[14] L. G. Villanueva *et al.*, "Surpassing fundamental limits of oscillators using nonlinear resonators," *Phys. Rev. Lett.*, vol. 110, no. 17, pp. 1–5, Apr. 2013.

[15] M. H. Matheny, M. Grau, L. G. Villanueva, R. B. Karabalin, M. C. Cross, and M. L. Roukes, "Phase synchronization of two anharmonic nanomechanical oscillators," *Phys. Rev. Lett.*, vol. 112, no. 1, pp. 1–5, Jan. 2014.

[16] C. Cassella and G. Piazza, "Low phase-noise autonomous parametric oscillator based on a 226.7 MHz AlN contour-mode resonator," *IEEE Trans. Ultrason., Ferroelectr., Freq. Control*, vol. 62, no. 4, pp. 617–624, Apr. 2015.

[17] D. Antonio, D. H. Zanette, and D. López, "Frequency stabilization in nonlinear micromechanical oscillators," *Nature Commun.*, vol. 3, no. 1, pp. 1–6, May 2012.

[18] E. Gavartin, P. Verlot, and T. J. Kippenberg, "Stabilization of a linear nanomechanical oscillator to its thermodynamic limit," *Nature Commun.*, vol. 4, no. 1, pp. 1–8, Dec. 2013.

[19] M. J. Seitner, M. Abdi, A. Ridolfo, M. J. Hartmann, and E. M. Weig, "Parametric oscillation, frequency mixing, and injection locking of strongly coupled nanomechanical resonator modes," *Phys. Rev. Lett.*, vol. 118, no. 25, pp. 1–6, Jun. 2017.

[20] E. Kenig *et al.*, "Optimal operating points of oscillators using nonlinear resonators," *Phys. Rev. E, Stat. Phys. Plasmas Fluids Relat. Interdiscip. Top.*, vol. 86, no. 5, pp. 1–8, Nov. 2012.

[21] C. Cassella, N. Miller, J. Segovia-Fernandez, and G. Piazza, "Parametric filtering surpasses resonator noise in ALN contour-mode oscillators," in *Proc. IEEE 27th Int. Conf. Micro Electro Mech. Syst. (MEMS)*, Jan. 2014, pp. 1269–1272.

[22] C. Cassella, S. Strachan, S. W. Shaw, and G. Piazza, "Phase noise suppression through parametric filtering," *Appl. Phys. Lett.*, vol. 110, no. 6, Feb. 2017, Art. no. 063503, doi: 10.1063/1.4975798.

[23] A. Suárez and R. Quéré, *Stability Analysis of Nonlinear Microwave Circuits*. Norwood, MA, USA: Artech House, 2003.

[24] A. Suárez, *Analysis and Design of Autonomous Microwave Circuits*. Hoboken, NJ, USA: Wiley, 2008, pp. 1–703.

[25] L. Pantoli, A. Suarez, G. Leuzzi, and F. Di Paolo, "Complete and systematic simulation tools for frequency divider design," *IEEE Trans. Microw. Theory Techn.*, vol. 56, no. 11, pp. 2442–2452, Nov. 2008.

[26] Z. Heshmati, I. C. Hunter, and R. D. Pollard, "Microwave parametric frequency dividers with conversion gain," *IEEE Trans. Microw. Theory Techn.*, vol. 55, no. 10, pp. 2059–2063, Oct. 2007.

[27] A. Suarez and R. Melville, "Simulation-assisted design and analysis of varactor-based frequency multipliers and dividers," *IEEE Trans. Microw. Theory Techn.*, vol. 54, no. 3, pp. 1166–1179, Mar. 2006.

[28] S. Jeon, A. Suárez, and D. B. Rutledge, "Nonlinear design technique for high-power switching-mode oscillators," *IEEE Trans. Microw. Theory Techn.*, vol. 54, no. 10, pp. 3630–3639, Oct. 2006.
[29] L. Pantoli and G. Leuzzi, "Stability analysis by conversion matrix and transient envelope simulations," in *Proc. Workshop Integr. Nonlinear Microw. Millim.-Wave Circuits (INMMiC)*, no. 2, 2010, pp. 123–126.
[30] L. Pantoli, G. Leuzzi, and F. Di Paolo, "Conversion matrix extraction by commercial CAD software for the stability design of autonomous circuits," *Int. J. RF Microw. Comput.-Aided Eng.*, vol. 20, no. 3, pp. 313–320, May 2010.
[31] L. Pantoli, G. Leuzzi, A. Santarelli, and F. Filicori, "Stability analysis and design criteria of paralleled-device power amplifiers under large-signal regime," *IEEE Trans. Microw. Theory Techn.*, vol. 64, no. 5, pp. 1442–1455, May 2016.
[32] L. Pantoli, D. Spina, D. Romano, G. Antonini, G. Leuzzi, and T. Dhaene, "Effective time-domain approach for the assessment of the stability characteristics and other non-linear effects of RF and microwave circuits," *IET Microw., Antennas Propag.*, vol. 13, no. 14, pp. 2470–2479, Nov. 2019.
[33] S. Hernandez and A. Suarez, "Systematic methodology for the global stability analysis of nonlinear circuits," *IEEE Trans. Microw. Theory Techn.*, vol. 67, no. 1, pp. 3–15, Jan. 2019.
[34] C. Cassella *et al.*, "Radio frequency angular momentum biased quasi-LTI nonreciprocal acoustic filters," *IEEE Trans. Ultrason., Ferroelectr., Freq. Control*, vol. 66, no. 11, pp. 1814–1825, Nov. 2019.
[35] D. Teeter, A. Platzker, R. Bourque, L. Street, and A. Ma, "WElE-6 oscillations in high power MMIC amplifiers," in *Int. Microw. Symp. Dig.*, 1999, pp. 967–970.
[36] K. Chawla and P. Shuth, "Harmonic and subharmonic filter," U.S. Patent 5 187 457, no. 19, Feb. 16, 1993.
[37] V. Iglesias, A. Suárez, and J. L. García, "New technique for the determination through commercial software of the stable-operation parameter ranges in nonlinear microwave circuits," *IEEE Microw. Guided Wave Lett.*, vol. 8, no. 12, pp. 424–426, Dec. 1998.
[38] P. M. Stevenson, "Optimized perturbation theory," *Phys. Rev. D, Part. Fields*, vol. 23, no. 12, pp. 2916–2944, Jun. 1981.
[39] A. Buonomo and A. Lo Schiavo, "Analyzing the dynamic behavior of RF oscillators," *IEEE Trans. Circuits Syst. I, Fundam. Theory Appl.*, vol. 49, no. 11, pp. 1525–1534, Nov. 2002.
[40] S. Strogatz, M. Friedman, A. J. Mallinckrodt, and S. McKay, "Nonlinear dynamics and chaos: With applications to physics, biology, chemistry, and engineering," *Comput. Phys.*, vol. 8, no. 5, p. 532, 1994, doi: 10.1063/1.4823332.
[41] F. C. Moon, "Experiments on chaotic motions of a forced nonlinear oscillator: Strange attractors," *J. Appl. Mech.*, vol. 47, no. 3, pp. 638–644, Sep. 1980.
[42] F. Ramirez, R. Melville, A. Suarez, and J. S. Kenney, "Nonlinear analysis and design of frequency selective limiters based on parametric circuits," in *IEEE MTT-S Int. Microw. Symp. Dig.*, Jun. 2008, pp. 947–950.
[43] G. R. Sloan, "The modeling, analysis, and design of filter-based parametric frequency dividers," *IEEE Trans. Microw. Theory Techn.*, vol. 41, no. 2, pp. 224–228, Feb. 1993.

Hussein M. E. Hussein (Student Member, IEEE) received the B.S. and M.Sc. degrees in electrical engineering from Cairo University, Giza, Egypt, in 2013 and 2017, respectively. He is currently pursuing the Ph.D. degree at the Department of Electrical and Computer Engineering, Northeastern University, Boston, MA, USA.

He is currently working on the development of parametric phase-noise reduction techniques, for RF systems, based on nonlinear devices and circuits.

Mahmoud A. A. Ibrahim (Student Member, IEEE) received the B.Sc. (Hons.) and M.Sc. degrees in electrical engineering from the Department of Electronics and Electrical Communications Engineering, Cairo University, Giza, Egypt, in 2013 and 2015, respectively. He is currently pursuing the Ph.D. degree in electrical engineering at Northeastern University, Boston, MA, USA.

From 2013 to 2015, he was a Teaching and Research Assistant with Cairo University. In the Summer of 2018, he joined the PLL Team, Qualcomm, San Diego, CA, USA, as an Analog-Mixed Signal Design Intern, where he was involved in the research and design of ultralow-power multigigahertz *LC* oscillators in deep-submicrometer Fin-FET technologies. Since 2016, he has been a Graduate Research and a Teaching Assistant with Northeastern University. He is also working on the design of ultralow-power transceivers for biomedical applications. His research interests include integrated analog, mixed-signal, and RF circuits for low-power wireless transceivers, and power management integrated circuits.

Giuseppe Michetti (Student Member, IEEE) received the B.S. and M.Sc. degrees from the Politecnico di Milano, Milan, Italy, in 2014 and 2018, respectively. He is currently pursuing the Ph.D. degree at the Department of Electrical and Computer Engineering, Northeastern University, Boston, MA, USA.

His research is based on MEMS applications for microwave circuits for mobile platforms. He is currently working on nonlinear and time-variant models and prototypes for RF circuits based on piezoelectric RF MEMS technologies for a novel generation of RF front ends.

Matteo Rinaldi (Senior Member, IEEE) received the Ph.D. degree in electrical and systems engineering from the University of Pennsylvania, Philadelphia, PA, USA, in December 2010.

He worked as a Post-Doctoral Researcher at the University of Pennsylvania in 2011. He joined the Department of Electrical and Computer Engineering, Northeastern University, Boston, MA, USA, as an Assistant Professor, in January 2012. He is currently an Associate Professor with the Department of Electrical and Computer Engineering, Northeastern University, where he is also the Director of the Northeastern SMART, a university research center that, by fostering the partnership between university, industry, and government stakeholders, aims to conceive and pilot disruptive technological innovation in devices and systems capable of addressing fundamental technology gaps in several fields, including the Internet of Things (IoT), 5G, quantum engineering, digital agriculture, robotics, and healthcare. He is the Founder and the CEO of Zepsor Technologies, Boston, USA, a startup company that aims to bring to market zero standby power sensors for various Internet-of-Things applications, including distributed wireless fire monitoring systems, battery-less infrared sensor tags for occupancy sensing, and distributed wireless monitoring systems of plant health parameters for digital agriculture. He is also the owner of Smart MicroTech Consulting LLC, Boston, USA, a company that routinely provides consulting services to government agencies, large companies, and startups in the broad areas of microtechnology and nanotechnology, Internet of Things, wireless communication devices and systems, radio frequency devices and systems, and sensors. His group has been actively working on experimental research topics and practical applications to ultralow-power MEMS/NEMS sensors (infrared, magnetic, chemical, and biological), plasmonic microelectromechanical and nanoelectromechanical devices, medical microsystems and implantable microdevices for intrabody networks, reconfigurable radio frequency devices and systems, phase change material switches, and 2-D material-enabled micromechanical and nanomechanical devices. The research in Dr. Rinaldi's group is supported by several federal grants (including DARPA, ARPA-E, NSF, and DHS), the Bill and Melinda Gates Foundation, and the Keck Foundation with funding of more than $14M since 2012. He has coauthored more than 140 publications in the aforementioned research areas and also holds ten patents and more than ten device patent applications in the field of MEMS/NEMS.

Dr. Rinaldi was a recipient of the IEEE Sensors Council Early Career Award in 2015, the NSF CAREER Award in 2014, the DARPA Young Faculty Award in 2012, the Best Student Paper Award at the 2009, 2011, 2015 (with his student), and 2017 (with his student) IEEE International Frequency Control Symposiums, the Outstanding Paper Award at the 18th International Conference on Solid-State Sensors, Actuators and Microsystems, Transducers 2015 (with his student), and the Outstanding Paper Award at the 32nd IEEE International Conference on Micro Electro Mechanical Systems, MEMS 2019 (with his student).

Marvin Onabajo (Senior Member, IEEE) received the B.S. degree *(summa cum laude)* in electrical engineering from The University of Texas at Arlington, Arlington, TX, USA, in 2003, and the M.S. and Ph.D. degrees in electrical engineering from Texas A&M University, College Station, TX, USA, in 2007 and 2011, respectively.

From 2004 to 2005, he was an Electrical Test/Product Engineer with Intel Corporation, Hillsboro, OR, USA. He joined the Analog and Mixed-Signal Center, Texas A&M University, in 2005, where he was engaged in research projects involving analog built-in testing, data converters, and on-chip temperature sensors for thermal monitoring. In Spring 2011, he worked as a Design Engineering Intern at the Broadband RF/Tuner Development Group at Broadcom Corporation, Irvine, CA, USA. He has been with Northeastern University, Boston, MA, USA, since Fall 2011, where he is currently an Associate Professor with the Department of Electrical and Computer Engineering. His research areas are analog/RF integrated circuit design, on-chip built-in testing and calibration, mixed-signal integrated circuits for medical applications, data converters, and on-chip sensors for thermal monitoring.

Dr. Onabajo received the 2015 CAREER Award from the National Science Foundation, the 2017 Young Investigator Program Award from the Army Research Office (ARO), and the 2015 Martin Essigman Outstanding Teaching Award from the College of Engineering at Northeastern University. He serves as an Associate Editor on the Editorial Board for the IEEE TRANSACTIONS ON CIRCUITS AND SYSTEMS—I: REGULAR PAPERS (TCAS-I, from 2016 to 2017, 2018 to 2019, and 2020 to 2021) and the *IEEE Circuits and Systems Magazine* (from 2016 to 2017, 2018 to 2019, and 2020 to 2021). From 2014 to 2015, he was on the Editorial Board of the IEEE TRANSACTIONS ON CIRCUITS AND SYSTEMS—II: EXPRESS BRIEFS (TCAS-II).

Cristian Cassella (Member, IEEE) received the B.S.E. and M.Sc. degrees (Hons.) from the University of Rome-Tor Vergata, Rome, Italy, in 2006 and 2009, respectively, and the Ph.D. degree from Carnegie Mellon University, Pittsburgh, PA, USA, in 2015.

In 2011, he was a Visiting Scholar with the University of Pennsylvania, Philadelphia, PA, USA. In 2015, he was a Post-Doctoral Research Associate with Northeastern University, Boston, MA, USA, where he is currently an Assistant Professor with the Department of Electrical and Computer Engineering. In 2016, he became an Associate Research Scientist. He is the author of 60 publications in peer-reviewed journals and conference proceedings. Two of his peer-reviewed journal articles published on the IEEE JOURNAL OF MICROELECTROMECHANICAL SYSTEMS (JMEMS) were selected as papers of excellent quality (JMEMS RightNowPapers), hence being released as open access. One of his journal articles was chosen as the cover for the *Nature Nanotechnology* October 2017 issue. He holds two patents and three patent applications in the areas of acoustic resonators and RF systems.

He received the Best Paper Award at the IEEE International Frequency Control Symposium, Prague, 2013. In 2018, he was a recipient of the Marie-Sklodowska-Curie Individual Fellowship from the European Community (EU). He is a technical reviewer for several journals, such as *Applied Physics Letters*, the IEEE TRANSACTIONS ON ELECTRON DEVICES, the IEEE TRANSACTIONS ON ULTRASOUND, FERROELECTRIC AND FREQUENCY CONTROL, the IEEE JMEMS, the IEEE ELECTRON DEVICE LETTER, the *Journal of Micromachine and Micro-Engineering*, the *Journal of Applied Physics*, the IEEE SENSORS LETTERS, and *Review of Scientific Instruments*.